Volume 179, Number 11, November 2006

JOURNAL OF
SOLID STATE
CHEMISTRY

www.elsevier.com/locate/jssc

CONTENTS

Abstracted/indexed in BioEngineering Abstracts, Chemical Abstracts, Coal Abstracts, Current Contents/Physics, Chemical, & Earth Sciences, Engineering Index, Research Alert, SCISEARCH, Science Abstracts, and Science Citation Index. Also covered in the abstract and citation database SCOPUS®. Full text available on ScienceDirect®.

Regular Articles

$(NH_3CH_2CH_2NH_3)B_6O_9(OH)_2$: Synthesis and crystal structure of a novel layered borate templated by ethylenediamine

Min Li, Jiazhong Chang, Zhenling Wang and Hengzhen Shi

Page 3265

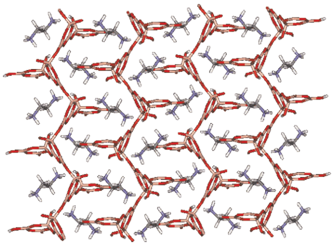

A novel intercalated borate compound $(NH_3CH_2CH_2NH_3)B_6O_9(OH)_2$ has been solvothermally synthesized and structurally characterized.

Synthesis of Ag-coated polystyrene colloids by an improved surface seeding and shell growth technique

Chungui Tian, Enbo Wang, Zhenhui Kang, Baodong Mao, Chao Zhang, Yang Lan, Chunlei Wang and Yanli Song

Page 3270

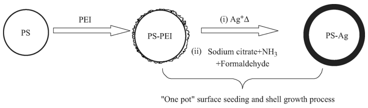

An improved surface seeding and shell growth technique was developed to prepare Ag-polystyrene core shell composite. The optical properties of the Ag-PS colloids could be tailored by changing the coverage of Ag.

Structural phase transitions in BaV_6O_{11}

Karen Friese and Yasushi Kanke

Page 3277

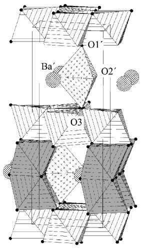

The structure of BaV_6O_{11} at 293 K. Octahedra around V(1) and trigonal bipyramids around V(3) are indicated. $V(2)O_6$ octahedra are only shown in the lower part; large hatched circles represent Ba-atoms.

Regular Articles—Continued

Charge states of Ca atoms in *β*-dicalcium silicate

Kazuhiro Mori, Ryoji Kiyanagi, Masao Yonemura, Kenji Iwase, Takashi Sato, Keiji Itoh, Masaaki Sugiyama, Takashi Kamiyama and Toshiharu Fukunaga

Page 3286

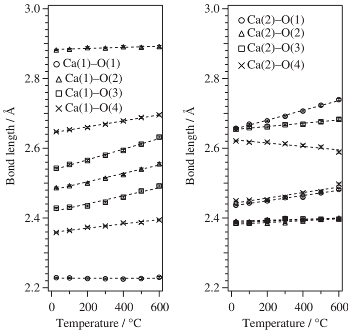

Temperature dependences of: (a) Ca(1)–O bond lengths, (b) Ca(2)–O bond angle. The broken straight lines are guides to the eyes.

A conjoint XRD–ND analysis of the crystal structures of austenitic and martensitic $Ti_{0.64}Zr_{0.36}Ni$ hydrides

F. Cuevas, M. Latroche, F. Bourée-Vigneron and A. Percheron-Guégan

Page 3295

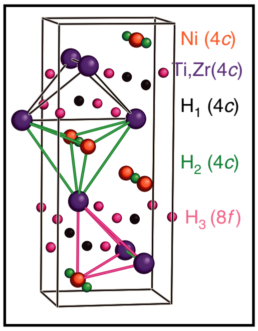

Hydrogen location and crystal structure of martensitic $Ti_{0.64}Zr_{0.36}Ni$ hydrides.

Neutron diffraction study on protonated and hydrated layered perovskite

Shunsuke Nishimoto, Motohide Matsuda, Stefanus Harjo, Akinori Hoshikawa, Toru Ishigaki, Takashi Kamiyama and Michihiro Miyake

Page 3308

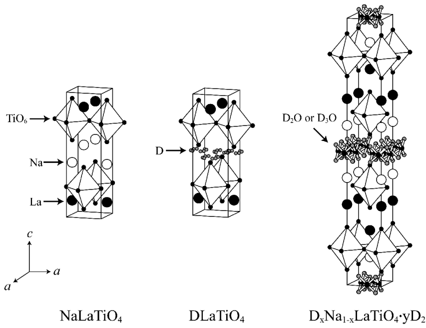

Schematic illustrations of the crystal structures of (a) NaLaTiO4, (b) $DLaTiO_4$ and (c) $D_{0.34}Na_{0.66}LaTiO_4$ $0.59D_2O$.

One-step synthesis of dispersed bimetallic carbides and nitrides from transition metals hexamethylenetetramine complexes

Sandra Chouzier, Pavel Afanasiev, Michel Vrinat, Tivadar Cseri and Magalie Roy-Auberger

Page 3314

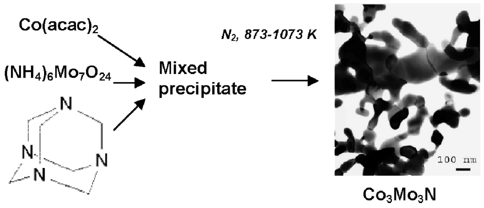

Bimetallic nitrides and carbides Co(Ni)–Mo were obtained from the decomposition of metals complexes with hexamethylenetetramine (HMTA) under inert atmosphere. During the decomposition, HMTA acts at once as a reducing agent and as a source of carbon and nitrogen. The method provides a simple one-step way to highly divided nitrides and carbides.

Densely packed single-crystal $Bi_2Fe_4O_9$ nanowires fabricated from a template-induced sol–gel route

Zhi Yang, Yi Huang, Bin Dong, Hu-Lin Li and San-Qiang Shi

Page 3324

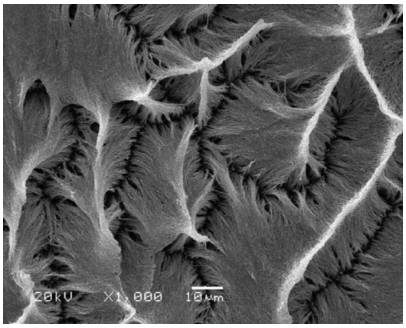

The top view in low magnification of SEM images of $Bi_2Fe_4O_9$ nanowires after AAO template is partly dissolved.

A study of the reactivity of elemental Cr/Se/Te thin multilayers using X-ray reflectometry, in situ X-ray diffraction and X-ray absorption spectroscopy

Malte Behrens, Jan Tomforde, Enno May, Ragnar Kiebach, Wolfgang Bensch, Dietrich Häußler and Wolfgang Jäger

Page 3330

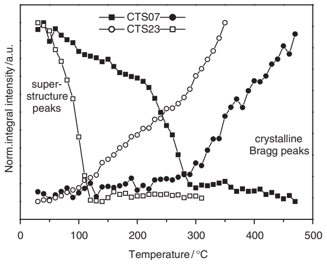

The first step of the reaction of elemental Cr/Te/Se multilayers is the interdiffusion of the elements as evidenced by the decay of the modulation peaks in the low-angle region of the X-ray diffraction patterns. The subsequent growth of Bragg peaks at higher scattering angles indicates crystallization of chromium chalcogenide $Cr_2Te_{3-x}Se_x$.

Isothermal kinetic of phase transformation and mixed electrical conductivity in Bi_3NbO_7

X.P. Wang, G. Corbel, S. Kodjikian, Q.F. Fang and P. Lacorre

Page 3338

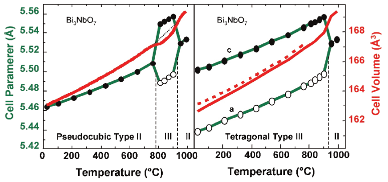

The metastable type-II form of Bi_3NbO_7, whose phase transformation kinetics to type-III form is studied in isothermal conditions, is shown to have a larger volume and a lower anionic (and electronic) conductivity than the type-III form of this fluorite-type bismuth niobate.

Oxygen permeability, thermal expansion and mixed conductivity of $Gd_xCe_{0.8-x}Pr_{0.2}O_{2-\delta}$, $x = 0, 0.15, 0.2$

D.P. Fagg, I.P. Marozau, A.L. Shaula, V.V. Kharton and J.R. Frade

Page 3347

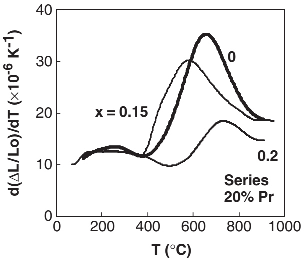

The differential of the thermal expansion plot clarifying the observation that the large increase in thermal expansion rate at intermediate temperatures is diminished with increasing x in the system $Gd_xCe_{0.8-x}Pr_{0.2}O_{2-\delta}$, for $x = 0$, 0.15 and 0.2.

Continued

Local environments and dynamics of hydrogen atoms in protonated forms of ion-exchangeable layered perovskites estimated by solid-state ^{1}H NMR

Shinsuke Tani, Yoshihiko Komori, Shigenobu Hayashi and Yoshiyuki Sugahara

Page 3357

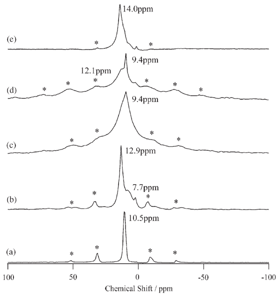

Solid-state ^{1}H MAS NMR spectra of protonated forms of ion-exchangeable layered perovskites: (a) $H[LaNb_2O_7]$; (b) $H[LaTa_2O_7]$; (c) $H_{1.8}[(Sr_{0.8}Bi_{0.2})Ta_2O_7]$; (d) $H_2[SrTa_2O_7]$; and (e) $H_2[La_2Ti_3O_{10}]$. The spinning side bands are marked with asterisks.

High pressure synthesis, crystal, magnetic structure and magnetotransport of $SrFe_{0.5}Co_{0.5}O_{3-\delta}$

A. Muñoz, J.A. Alonso, M.J. Martínez-Lope, C. de la Calle and M.T. Fernández-Díaz

Page 3365

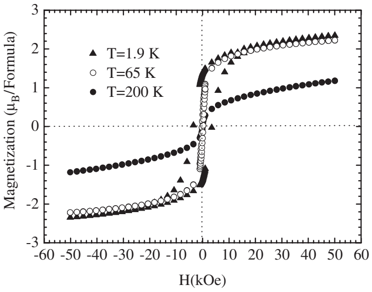

$SrFe_{0.5}Co_{0.5}O_{2.88}$ is a simple cubic perovskite at 2 and 295 K, ferromagnetic (FM) with $T_C \approx 330$ K. Neutron diffraction data show that the magnetic structure is collinear and characterized by a propagation vector $\mathbf{k} = 0$. It exhibits a magnetorresistance of 6.5% at 5 K.

Temperature-dependent crystallographic studies and electronic structure of $Ba_2Cd_3Bi_4$

Sheng-qing Xia and Svilen Bobev

Page 3371

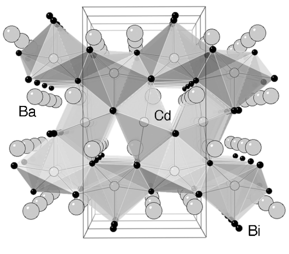

$Ba_2Cd_3Bi_4$ in *Cmce*

$Ba_2Cd_3Bi_4$, a long-known ternary intermetallic phase whose structure had not been well characterized, was reexamined and the structure refined at four different temperatures. The study proved the existence of a small position disorder, associated with the weakly bound Cd atoms.

Sm_2NiSn_4: The intermediate structure type between $ZrSi_2$ and $CeNiSi_2$

Zhong-Ming Sun, Da-Chun Pan, Xiao-Wu Lei and Jiang-Gao Mao

Page 3378

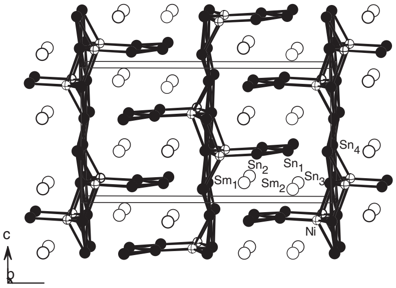

A new rare earth nickel stannide, Sm_2NiSn_4, has been prepared by the solid-state reactions of the corresponding pure elements at high temperature in welded tantalum tubes. Its structure can be viewed as the intermediate type between $ZrSi_2$ and $CeNiSi_2$. Sm_2NiSn_4 features 2D corrugated $[NiSn_4]^{6-}$ layers in which the 1D Sn zigzag chains and the 2D Sn square sheets are bridged by Ni atoms. Results of both resistivity measurements and extended-Hückel tight-binding band structure calculations indicate that Sm_2NiSn_4 is metallic.

Structural characterization of the Ta-rich part of the Ta–Al system

A. Boulineau, J.-M. Joubert and R. Černý

Page 3385

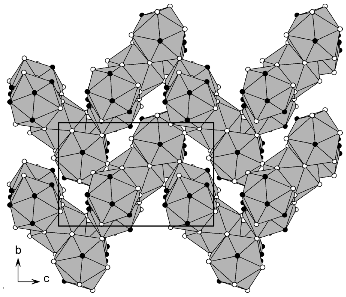

Crystal structure of the β Ta–Al phase.

Two metal chalcogenides, $Hg_2Te_2X_2$ (X = Br, I): 3-D framework constructed from novel left-handed helices

Wen-Tong Chen, Ming-Sheng Wang, Zhang-Jing Zhang, Gang Xu, Guo-Cong Guo and Jin-Shun Huang

Page 3394

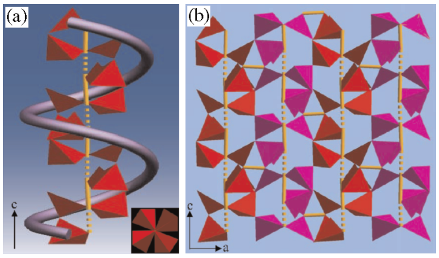

A new family of *IIB*$_2Q_2X_2$ system, possessing an acentric nature that allows them to be a potential NLO material, has been synthesized via solid-state reactions. The crystal structures are characterized by a 3-D framework structure, comprising of interconnected left-handed helices. Optical absorption spectra show that both compounds are excellent candidate for potential photoelectric materials.

Synthesis and characterization of a new open-framework fluorinated gallium phosphite with three-dimensional intersecting channels

Li Wang, Tianyou Song, Yong Fan, Zhenfen Tian, Ying Wang, Suhua Shi and Jianing Xu

Page 3400

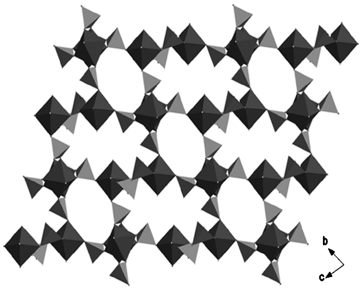

$(C_4N_2H_{12})[Ga_2F_3(HPO_3)_2(H_2PO_3)]$ **1** is a new open-framework fluorinated gallium phosphite with four intersecting channels running throughout the structure as 8, 12-member ring channels along to the *a*-axis and 12-member ring channels along the *b*- and *c*-axis, respectively.

Cerium effect on the phase structure, phase stability and redox properties of Ce-doped strontium ferrates

F. Deganello, L.F. Liotta, A. Longo, M.P. Casaletto and M. Scopelliti

Page 3406

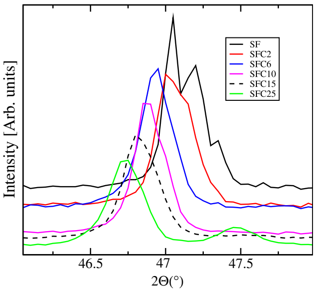

The Ce-doped $SrFeO_3$ structure changes with cerium content: undoped $SrFeO_3$ is tetragonal ($I/4mmm$), 2 mol%-doped $SrFeO_3$ is still tetragonal with higher symmetry ($P/4mmm$), whereas from 6 to 15 mol% the structure becomes pure cubic. The cubic (or pseudo-cubic) reticular constant increases with cerium content.

Crystal structure and phase transformations of calcium yttrium orthophosphate, $Ca_3Y(PO_4)_3$

Koichiro Fukuda, Tomoyuki Iwata and Takahiro Niwa

Page 3420

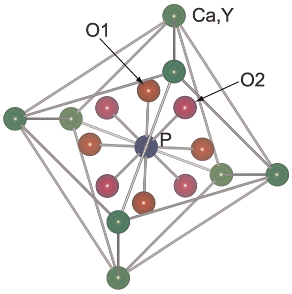

Part of the $Ca_3Y(PO_4)_3$ structure, viewed along [001].

A computational study into the (tetrahedral) distortion of TX_2 α-quartz materials: The effect of changing the chemical composition away from SiO_2

Martijn A. Zwijnenburg, Robert Huenerbein, Robert G. Bell and Furio Corà

Page 3429

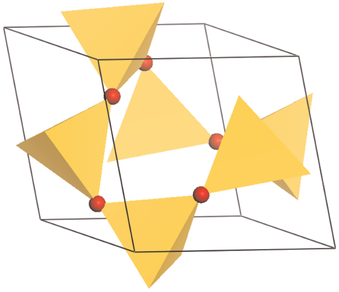

View on a quartz unit-cell with TX_4 tetrahedra.

Phase relations and crystal structures in the systems $(Bi,Ln)_2WO_6$ and $(Bi,Ln)_2MoO_6$ (Ln = lanthanide)

Peter S. Berdonosov, Dmitri O. Charkin, Kevin S. Knight, Karen E. Johnston, Richard J. Goff, Valeriy A. Dolgikh and Philip Lightfoot

Page 3437

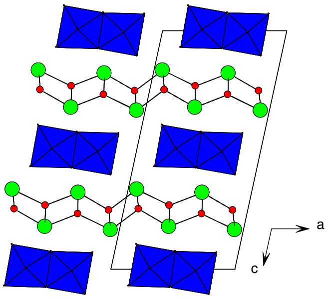

A summary of phase relations in the lanthanide-doped bismuth tungstate and bismuth molybdate systems is presented, together with some additional structural data on several of these phases.

Stability and oxide ion conductivity in rare-earth aluminium cuspidines

M.C. Martín-Sedeño, D. Marrero-López, E.R. Losilla, S. Bruque, P. Núñez and M.A.G. Aranda

Page 3445

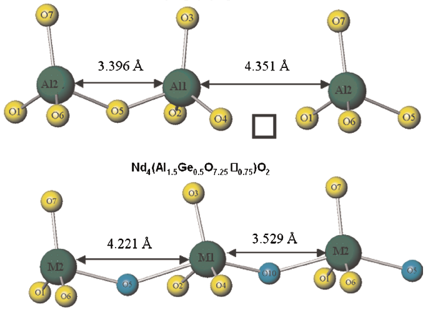

The attached figure shows the changes in the oxygen distribution of oxy-cuspidines determined by neutron powder diffraction. These oxo-salts are oxide ion conductors with negligible electronic contribution.

Continued

Two new binary lanthanide polytellurides: Syntheses and crystal structures of $CeTe_{1.90}$ and $SmTe_{1.80}$

Ismail Ijjaali and James A. Ibers

Page 3456

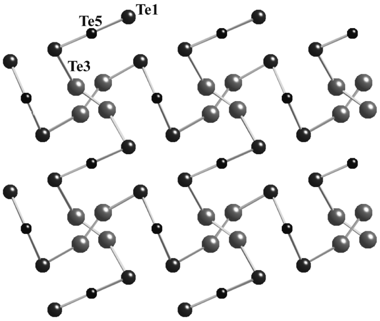

A Te net in $SmTe_{1.80}$.

Synthesis, structure and magnetic properties of new phosphates $K_2Mn_{0.5}Ti_{1.5}(PO_4)_3$ and $K_2Co_{0.5}Ti_{1.5}(PO_4)_3$ with the langbeinite structure

Ivan V. Ogorodnyk, Igor V. Zatovsky,
Nikolay S. Slobodyanik, Vyacheslav N. Baumer and
Oleg V. Shishkin

Page 3461

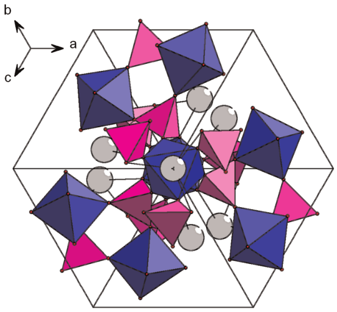

A view of langbeinite structure in direction perpendicular to [111].

Subsolidus phase equilibria and properties in the system Bi_2O_3:$Mn_2O_{3\pm x}$:Nb_2O_5

T.A. Vanderah, M.W. Lufaso, A.U. Adler, I. Levin,
J.C. Nino, V. Provenzano and P.K. Schenck

Page 3467

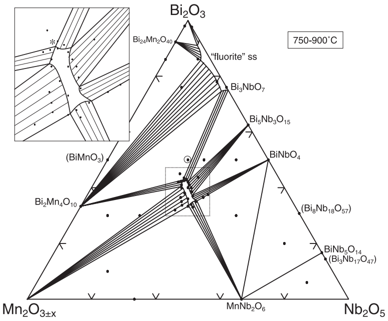

Ternary compound formation in the Bi–Mn–Nb–O system is limited to a pyrochlore solid solution which occurs at "Bi-deficient" stoichiometries compared to conventional $A_2B_2O_7$-type formulations with Bi on the A-sites and Mn/Nb on the B-sites—all pyrochlores in this system exhibit displacive structural behavior.

Defect microstructures of TiO_2 rutile due to Zr^{4+} dissolution and expulsion

K.C. Yang, P. Shen and D. Gan

Page 3478

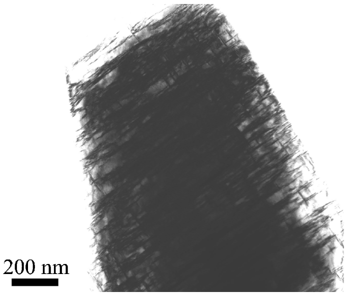

TEM image of Zr-doped rutile viewed along its *c*-axis showing two variants of plate-like precipitates formed during aging at 900 °C for 200 h.

The mixed valent tellurate $SrTe_3O_8$: Electronic lone pair effect of Te^{4+}

N. Barrier, S. Malo, O. Hernandez, M. Hervieu and
B. Raveau

Page 3484

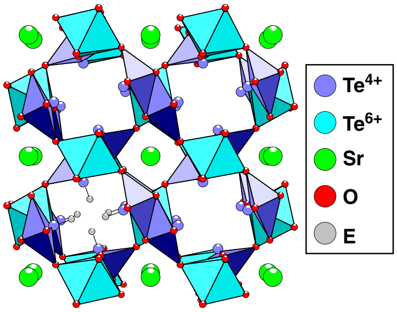

Tunnel structure of the mixed valent tellurate $SrTe_3O_8$ determined *ab initio* against powder X-ray diffraction; structure viewed along [001] direction with *E* the electronic lone pairs of the Te^{4+} cations.

Structure property relationships in the ATi_2O_4 (A = Na, Ca) family of reduced titanates

Margret J. Geselbracht, Ann S. Erickson, Matthew P. Rogge,
John E. Greedan, Richard I. Walton, Matthew W. Stoltzfus,
Hank W. Eng and Patrick M. Woodward

Page 3489

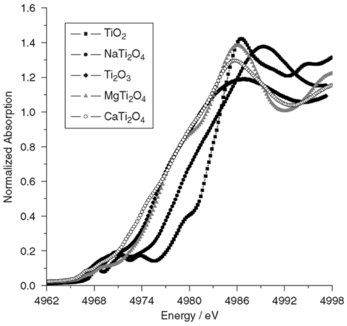

Normalized titanium K-edge XANES spectra confirm mixed-valence for $NaTi_2O_4$ with an edge energy intermediate between Ti^{3+} oxides such as $CaTi_2O_4$, $MgTi_2O_4$ and Ti_2O_3, and Ti^{4+} containing oxides such as TiO_2.

Hydrothermal synthesis of a luminescent Europium(III) sulfate with three-dimensional chiral framework structure

Chuan-De Wu and Zi-Yang Liu

Page 3500

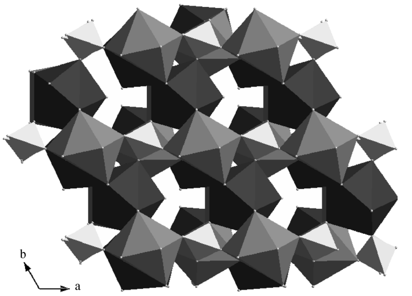

The hydrothermal reaction of Eu_2O_3, Na_2SO_4 in acidified aqueous solution afforded a chiral three-dimensional framework compound $[NaEu(H_2O)(SO_4)_2]$ (**1**), which is composed of three kinds of right-handed helical chains $\{EuOSO_4\}$, $\{NaOSO_4\}$ and $\{EuONa\}$. The luminescent properties of **1** are also studied and analyzed.

High-temperature neutron diffraction study of the cation ordered perovskites $TbBaMn_2O_{5+x}$ and $TbBaMn_2O_{5.5-y}$

Elizabeth Castillo-Martínez, Anthony J. Williams and J. Paul Attfield

Page 3505

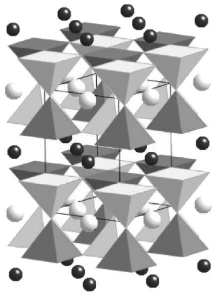

In situ powder neutron diffraction shows that, surprisingly, there is no miscibility between $TbBaMn_2O_{5+x}$ and the oxygen intercalated product $TbBaMn_2O_{5.5-y}$ up to 600 °C. $TbBaMn_2O_5$ is Mn^{2+}/Mn^{3+} charge ordered and any charge melting transition occurs > 600 °C. This charge ordering is remarkably robust in comparison to that in other oxides.

Extending framework based on the linear coordination polymers: Alternative chains containing lanthanum ion and acrylic acid ligand

Hui Li, Ming Guo, Hong Tian, Fei-Yue He, Gene-Hsiang Lee and Shie-Ming Peng

Page 3511

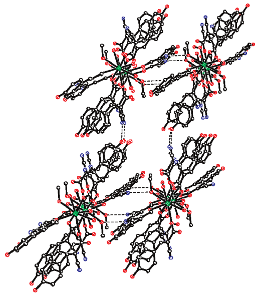

3D H-bonding network directed by the ligand based on the rare alternative chain of lanthanum complex containing *syn–syn* and *anti–syn* coordination mode of α-cyano-4-hydroxycinnamic acid.

Structural and compositional variations in Ta_3N_5 produced by high-temperature ammonolysis of tantalum oxide

Stuart J. Henderson and Andrew L. Hector

Page 3518

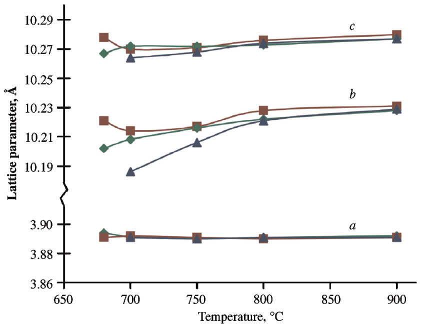

One crystallographic nitrogen site in Ta_3N_5 varies markedly in composition with preparation conditions, the effect of this is seen in the *b*-axis length and optical properties.

Incommensurate modulated structure of the ferromagnetic shape-memory Ni_2MnGa martensite

Lara Righi, Franca Albertini, Gianluca Calestani, Luigi Pareti, Antonio Paoluzi, Clemens Ritter, Pedro A. Algarabel, Luis Morellon and M. Ricardo Ibarra

Page 3525

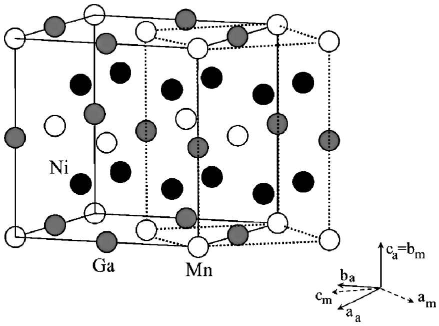

Perspective view of the $L2_1$ cubic structure of Ni_2MnGa austenite. The dotted lines define the basic structure of the incommensurate modulated martensite.

Synthesis and electrochemical properties of nonstoichiometric $LiAl_xMn_{2-x}O_{4-\delta}$ as cathode materials for rechargeable lithium ion battery

Woosuk Cho, Wonkyung Ra, Junichi Shirakawa, Masanobu Nakayama and Masatake Wakihara

Page 3534

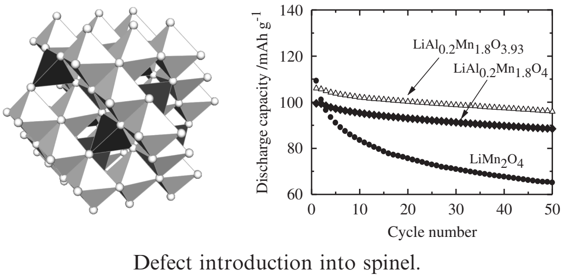

Defect introduction into spinel.

Continued

The new silver(I)thioantimonate(III) $[C_4N_2H_{14}][Ag_3Sb_3S_7]$ and a new structural variant of the silver(I)thioantimonate(III) $[C_2N_2H_9]_2[Ag_5Sb_3S_8]$ both synthesized under solvothermal conditions

V. Spetzler, C. Näther and W. Bensch

Page 3541

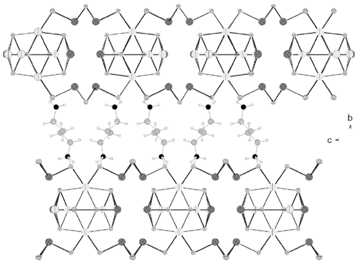

In the new silver thioantimonate $[C_4N_2H_{14}][Ag_3Sb_3S_7]$ the layered $[Ag_3Sb_3S_7]^{2-}$ anion is constructed by two different chains. An $[Sb_2S_4]$ chain is formed by vertex sharing of SbS_3 pyramids. The second chain contains Ag_3SbS_5 group which are connected by S atoms. The layered anion is obtained by condensation of the two individual chains. The organic structure director is sandwiched by the inorganic layers and the shortest inter-layer distance is about 6.4 Å.

Synthesis, characterization and crystal structure of $K_2Bi(PO_4)(MoO_4)$

Igor V. Zatovsky, Katherina V. Terebilenko, Nikolay S. Slobodyanik, Vyacheslav N. Baumer and Oleg V. Shishkin

Page 3550

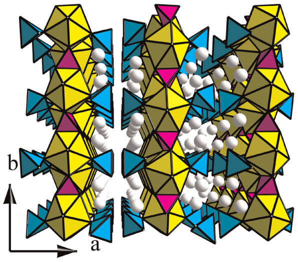

Stereo view of structure $K_2Bi(PO_4)(MoO_4)$ along the *c* direction.

Compression mechanisms of symmetric and Jahn–Teller distorted octahedra in double perovskites: A_2CuWO_6 (A = Sr, Ba), Sr_2CoMoO_6, and La_2LiRuO_6

Michael W. Lufaso, William R. Gemmill, Samuel J. Mugavero III, Yongjae Lee, Thomas Vogt and Hans-Conrad zur Loye

Page 3556

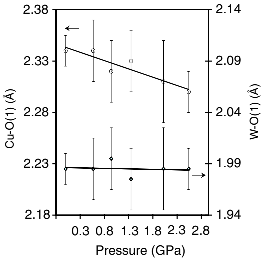

Preferential compression of long Cu–O bonds, resulting from Jahn–Taller distortions aligned parallel to the *c*-axis, is observed for Ba_2CuWO_6. This in contrast to the compression mechanism often observed in perovskites, i.e., octahedral tilting and symmetric octahedral bond compression.

Alkaline hydrolysis of dimethyl terephthalate in the presence of $[LiAl_2(OH)_6]Cl \cdot 2H_2O$

Lixu Lei, Weifeng Zhang, Meng Hu and Hegen Zheng

Page 3562

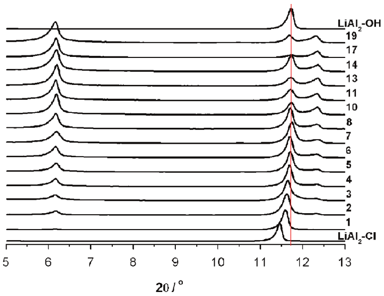

XRD patterns of the solid products of the alkaline hydrolysis of dimethyl terephthalate (DMT) in the presence of $[LiAl_2(OH)_6]Cl$ at 70 °C halted at different time, which shows that $[LiAl_2(OH)_6]Cl$ turns out to be $[LiAl_2(OH)_6]OH$, and $[LiAl_2(OH)_6]_2TP$ forms gradually. In this reaction, the alkaline hydrolysis of DMT is controlled by replacement of Cl^- in $[LiAl_2(OH)_6]Cl$ by OH^-, and subsequent replacement of OH^- in $[LiAl_2(OH)_6]OH$ by terephthalate anion.

The nature of the orthorhombic to tetragonal phase transition in $Sr_{1-x}Ca_xMnO_3$

Qingdi Zhou and Brendan J. Kennedy

Page 3568

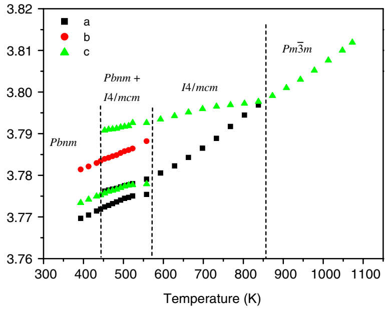

The temperature dependence of the lattice parameters for $Sr_{0.5}Ca_{0.5}MnO_3$.

Magnetic properties of lanthanide rhenium oxides Ln_3ReO_7 (Ln = Sm, Eu, Ho)

Makoto Wakeshima and Yukio Hinatsu

Page 3575

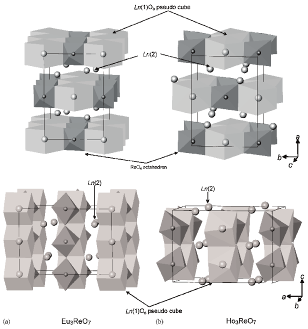

Crystal structures of Eu_3ReO_7 (a) and Ho_3ReO_7 (b). Sm_3ReO_7 shows an antiferromagnetic transition at 1.9 K, and Eu_3ReO_7 indicates a magnetic anomaly at 12 K. Both compounds undergo a structure transition at 270 and 350 K, respectively.

Rapid Communications

A novel orange phosphor of Eu^{2+}-activated calcium chlorosilicate for white light-emitting diodes

Weijia Ding, Jing Wang, Mei Zhang, Qiuhong Zhang and Qiang Su

Page 3582

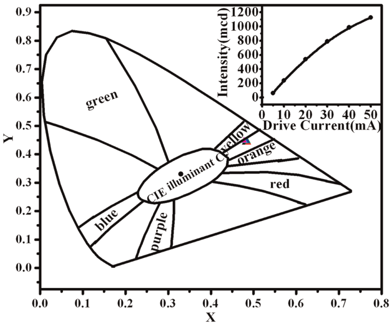

The CIE coordinates of as-synthesized and orange LED-based CSCE under $I_F = 5.0$, 10, 20, 30, 40, 50 mA in the CIE 1931 chromaticity diagram. The inset shows the dependence of the emission intensity on forward-bias currents.

Hydroxide flux synthesis and crystal structure of the ordered palladate, $LuNaPd_6O_8$

Samuel J. Mugavero III, Mark D. Smith and Hans-Conrad zur Loye

Page 3586

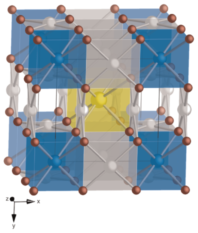

Unit cell of the ordered palladate $LuNaPd_6O_8$ viewed along the z-direction. The Pd^{2+} cations (grey) reside in a square planar coordination environment and bridge together the LuO_8 (blue) and NaO_8 (yellow) cubes.

Erratum

Erratum to “Structural change in a series of protonated layered perovskite compounds, $HLnTiO_4$ (Ln = La, Nd and Y)” [J. Solid State Chem. 179 (2006) 1892–1897]

Shunsuke Nishimoto, Motohide Matsuda, Stefanus Harjo, Akinori Hoshikawa, Takashi Kamiyama, Toru Ishigaki and Michihiro Miyake

Page 3590

Author inquiries

Submissions

For detailed instructions on the preparation of electronic artwork, consult Elsevier’s Author Gateway at http://authors.elsevier.com.

Other inquiries

Visit Elsevier’s Author Gateway (http://authors.elsevier.com) for the facility to track accepted articles and set up e-mail alerts to inform you of when an article’s status has changed. The Author Gateway also provides detailed artwork guidelines, copyright information, frequently asked questions and more.

Contact details for questions arising after acceptance of an article, especially those relating to proofs, are provided after registration of an article for publication.

Language Polishing

Authors who require information about language editing and copyediting services pre- and post-submission should visit http://www.elsevier.com/wps/find/authorshome.authors/languagepolishing or contact authorsupport@elsevier.com for more information. Please note Elsevier neither endorses nor takes responsibility for any products, goods, or services offered by outside vendors through our services or in any advertising. For more information please refer to our Terms & Conditions at http://www.elsevier.com/wps/find/termsconditions.cws_home/termsconditions.

For a full and complete Guide for Authors, please refer to *J. Solid State Chem.,* Vol. 179, Issue 8, pp. *bmi–bmv*. The instructions can also be found at http://www.elsevier.com/wps/find/journaldescription.cws_home/622898/authorinstructions.

Journal of Solid State Chemistry has no page charges.